J of Astronaut Sci (2016) 63:237–262
DOI 10.1007/s40295-016-0090-4

Space Weather Influence on Relative Motion Control using the Touchless Electrostatic Tractor

Erik A. Hogan[1] · **Hanspeter Schaub**[1]

Published online: 6 July 2016

Abstract With recent interest in the use of electrostatic forces for contactless tugging and attitude control of noncooperative objects for orbital servicing and active debris mitigation, the need for a method of remote charge control arises. In this paper, the use of a directed electron beam for remote charge control is considered in conjunction with the relative motion control. A tug vehicle emits an electron beam onto a deputy object, charging it negatively. At the same time, the tug is charged positively due to beam emission, resulting in an attractive electrostatic force. The relative position feedback control between the tug and the passive debris object is studied subject to the charging being created through an electron beam. Employing the nominal variations of the GEO space weather conditions across longitude slots, two electrostatic tugging strategies are considered. First, the electron beam current is adjusted throughout the orbit in order to maximize this resulting electrostatic force. This open-loop control strategy compensates for changes in the nominally expected local space weather environment in the GEO region to adjust for fluctuations in the local plasma return currents. Second, the performance impact of using a fixed electron beam current on the electrostatic tractor is studied if the same natural space weather variations are assumed. The fixed electron beam current shows a minor performance penalty (< 5 %) while providing a much simpler implementation that does not require any knowledge of local space weather conditions.

Keywords Electrostatic tractor · Spacecraft charging · Space debris mitigation

✉ Erik A. Hogan
erik.hogan@colorado.edu

[1] University of Colorado at Boulder, Boulder, CO 80309, USA

Introduction

Recently, interest in the use of electrostatic forces for contactless tugging and remote attitude control of noncooperative objects has grown [15, 28, 30, 34]. Originally proposed for space debris mitigation at geosynchronous (GEO) altitudes, the electrostatic tugging concept relies on a combination of an attractive electrostatic force between two craft and low thrusting capability on one of the craft [28]. The attractive force acts as a virtual tether between the two objects, and a low thrust maneuver is used to tow the noncooperative object into a new orbit [15]. Considering nonsymmetrical spacecraft geometries, the charging also gives rise to torques on the craft [19, 33]. Through careful manipulation of the charging histories, these torques can be applied in a manner sufficient to despin a noncooperative object remotely [30]. This latter ability greatly simplifies any orbital servicing mission where great efforts are required to first despin objects spinning at 1 degree per second or greater [8, 9].

Generally, a noncooperative object such as space debris or a defunct satellite requiring servicing will not possess the capability for self charge control. This dictates the need for a touchless method of remote charge transfer. To this end, a focused electron beam has been suggested as a means for achieving remote charge control for the electrostatic tugging application [29]. The tugging vehicle, equipped with an electron beam, approaches the target deputy object. By focusing the electron beam onto the deputy, a negative potential results from the bombardment of electrons. At the same time, the tug is charged positively by the emission of the electron beam, as illustrated in Fig. 1. This process generates the required attractive electrostatic force necessary for towing applications, or torques for despinning operations. It is worth noting that electron beams have been used as a method for self-charge control of spacecraft for decades [20, 23]. However, they have not been used to do active charging of a neighboring space object.

In this study, we restrict our attention to focus on the case of using an electron beam to achieve remote charge control. A similar process could be implemented using an ion beam. However, depending on the separation distance, a focused ion

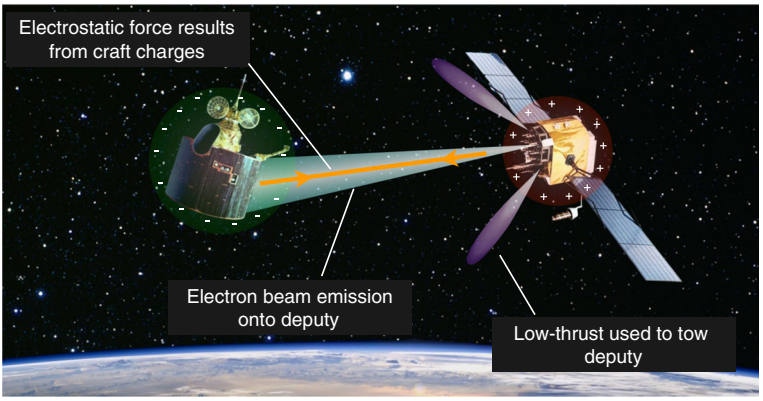

Fig. 1 Illustration of the electrostatic tugging concept

beam could impart more momentum on the deputy object than an electron beam due to the larger mass of ions relative to electrons [29]. As a result, the electrostatic force is less effective during tugging because it is partially countered by the resulting impulsive force generated by the ion bombardment. In fact, this resulting force is large enough that a directed ion beam has been proposed as a method for touchless deorbiting of space debris [3, 4]. With the electrostatic tractor application, the separation distances are considered to be less than 50 meters. The closer the object, the stronger the tractor will be. With this close separation range, the electron gun provides the preferred charging method. Further, the electron gun is a significantly simpler charge emission mechanism than an ion beam, which thus simplifies the electrostatic tractor design.

In [29], a simplified first-order analytical model is derived to compute the resulting charge levels on a tug and deputy spacecraft using an electron beam for charge transfer. The model incorporates the electron beam current, the electron and ion currents from the space plasma environment, the secondary electrons emitted by the deputy as a result of the electron beam impact, and the photoelectron currents. A single space weather condition is considered, and charging results as a function of beam current are computed assuming two spherical craft of equal radii. In the current study, this charging model is incorporated into a relative position feedback control strategy developed to maintain a sufficient electrostatic force for tugging in the face of changing space weather conditions. Treating electron beam current as the electrostatic tractor control variable, a current control strategy is applied that seeks to maximize the magnitude of the electrostatic force throughout a typical day in the life at GEO [11]. Because the plasma return currents impact the potentials on tug and deputy, changes in the local space weather conditions can increase or reduce the electrostatic forces experienced by the craft. This is compensated for by modifying the electron beam current.

The ultimate goal is choosing a beam current that generates the largest electrostatic tractor force for a debris tugging application. The GEO debris reorbiting scenario is used as the benchmark to see how this current control will impact the tractor performance. Modifying the current to generate the best possible tugging performance requires knowledge of the space weather environment, which may be difficult to obtain in real time. An alternative strategy would be to simply maintain a fixed beam current in the face of space weather variations. Perhaps the performance losses when compared to an ideal beam current are not significant enough to warrant the added complexity of a space weather dependent current formulation. The mean GEO space weather variations as discussed by [11] serve as a guide for identifying expected plasma conditions within an orbit. The mean GEO Debye lengths have been shown to range from less than 10 meters to several hundreds of meters, and increase and decrease with fluctuations in solar storm activity. Of particular interest to the electrostatic tractor performance are actually the prevailing quiet space weather conditions where the local GEO plasma is cold and dense. These conditions lead to small Debye lengths, and will have a stronger impact on the charging and electrostatic forces.

The paper is structured as follows. First, a brief review of the spacecraft charging model developed for the charge transfer process is presented. Next, an overview of the GEO space weather environment is presented, along with the plasma models used in

this study. Following that, a review of the sigma-set relative motion description is provided; the sigma-set is used later in the paper to develop the relative motion control strategy. Consideration of the space weather fluctuations is then used to develop an open-loop current control strategy. The variable current control scheme is then compared with a scenario where the current is held constant during the tugging maneuver. Lastly, numerical simulation is used to illustrate the impacts of these space weather fluctuations on the relative motion control and reorbiting performance.

Background

In this paper, a scenario is considered where a spacecraft (the tug) is equipped with an electron gun that is used for remote charging of a second satellite (the deputy). Due to the near proximity of tug and deputy, an electrostatic force is generated which is used in combination with low thrust to tow the deputy into a new orbit. In general, the deputy may be a cooperative spacecraft or a non-functioning debris object. Here, a baseline scenario of reorbiting a GEO debris object into a disposal orbit is considered. Only a semimajor axis change is required and the tug and deputy maintain a constant leader-follower position throughout the duration of the maneuver [15, 25]. The study utilizes a charging model that accounts for the numerous current sources experienced by a satellite in the space environment, incorporates space weather conditions adapted from observed values at GEO, and combines the charging model into a relative motion control scheme utilizing a recently developed relative orbital motion description.

Spacecraft Charging Model

The electrostatic tugging force used for towing is dependent on the charging that occurs on both the tug and deputy. Several factors influence this charging process. Naturally occurring ion and electron plasma currents are collected by the spacecraft, and photoelectrons may be emitted depending on the spacecraft potential and presence of sunlight. Focused electron beam emission by the tug is used for charge control. When the electron beam is absorbed by the deputy, secondary electron emission occurs as the incoming beam electrons excite and release electrons from the deputy surface material. The potential levels achieved by the tug and deputy result from a balance of these various current sources. To compute these potentials, the charging model developed in [29] is applied. Note that the numerical values used below for the various parameters in the charging model are taken directly from their work.

A photoelectron current occurs whenever the spacecraft are in sunlight. This current is modeled by

$$I_{ph}(\phi) = j_{ph,0} A_{\perp} e^{-\phi/T_{ph}} \qquad \phi > 0 \tag{1a}$$

$$= j_{ph,0} A_{\perp} \qquad \phi \leq 0 \tag{1b}$$

where ϕ is the spacecraft potential, $T_{ph} = 2$ eV is the temperature of the emitted photoelectrons, $j_{ph,0} = 20\ \mu\text{A/m}^2$ is the photoelectron flux, and $A_\perp$ is the cross-sectional area exposed to sunlight.

The plasma electron current is modeled by

$$I_e(\phi) = -\frac{Aqn_e w_e}{4} e^{\phi/T_e} \qquad \phi < 0 \tag{2a}$$

$$= -\frac{Aqn_e w_e}{4}\left(1 + \frac{\phi}{T_e}\right) \qquad \phi \geq 0, \tag{2b}$$

where A is the surface area exposed to the plasma environment, T_e is the plasma electron temperature, n_e is the plasma electron density, q is the elementary charge, and $w_e = \sqrt{8T_e/\pi m_e}$ is the thermal velocity of the electrons. The electron mass is represented by m_e. Similarly, the plasma ion current is computed using

$$I_i(\phi) = \frac{Aqn_i w_i}{4} e^{-\phi/T_i} \qquad \phi > 0 \tag{3a}$$

$$= \frac{Aqn_i w_i}{4}\left(1 - \frac{\phi}{T_i}\right) \qquad \phi \leq 0, \tag{3b}$$

where $w_i = \sqrt{8T_i/\pi m_i}$. Note that the variable quantities represent the same parameters as before, except the subscript i is used to denote they represent ions. In the space weather model for the GEO environment utilized here, the ion species consists solely of protons.

Charge control is achieved using an electron emitted from the tug onto the deputy. A portion of the beam current will be absorbed by the debris, depending on tug pointing accuracy and the charge levels of both tug and debris. This current is modeled as

$$I_D(\phi_D) = -\alpha I_t \qquad q\phi_T - q\phi_D < E_{EB} \tag{4a}$$

$$= 0 \qquad q\phi_T - q\phi_D \geq E_{EB}, \tag{4b}$$

where I_t is the beam current emitted by the tug, E_{EB} is the electron beam energy, and the subscripts T and D represent the tug and deputy, respectively. The parameter α represents the efficiency of the charge transfer process; it is the fraction of the beam current emitted by the tug that reaches the deputy. In general, this is a function of beam pointing accuracy and the width of the beam at the deputy location. It can also be impacted by the tug and debris potentials, in addition to the beam energy. In the current paper a value of $\alpha = 1$ is used, which maintains the value established in [29]. This assumes a well focused and accurately pointed beam. Better quantification of the α parameter is beyond the scope of this paper, and is left for future work.

When the electron beam impacts the deputy object, the incoming electrons result in the emission of secondary electrons. Because of the large negative potential of the debris object (kV level), these electrons will escape. This represents a significant

current source that must be accounted for. Secondary electron emission is modeled by [12]

$$I_{\mathrm{SEE}}(\phi_D) = -4Y_M I_D(\phi_D)\kappa \qquad \phi_D < 0 \tag{5a}$$

$$= 0 \qquad \phi_D \geq 0, \tag{5b}$$

where

$$\kappa = \frac{E_{\mathrm{eff}}/E_{\mathrm{max}}}{(1 + E_{\mathrm{eff}}/E_{\mathrm{max}})^2}$$

and $E_{\mathrm{eff}} = E_{EB} - q\phi_T + q\phi_D$. Y_M is the maximum yield of secondary electron production, and E_{max} is the impact energy at which this maximum occurs. In this paper, the values of $Y_M = 2$ and $E_{\mathrm{max}} = 300$ eV are used.

For the tug, the charging is dominated by the plasma electron current and electron beam emission. The tug settles to a potential that satisfies the current balance $I_e(\phi_T) + I_t = 0$. This is solved analytically as

$$\phi_T = \left(\frac{4I_t}{Aqn_e w_e} - 1\right) T_e, \tag{6}$$

which assumes a positive tug potential. This will be the case provided the beam current is sufficient. The current balance on the deputy object contains a few more contributions, and an analytical solution does not exist. The deputy will achieve a potential that satisfies

$$I_{\mathrm{Tot}} = I_e(\phi_D) + I_i(\phi_D) + I_{\mathrm{SEE}}(\phi_D) + I_{ph}(\phi_D) + I_D(\phi_D) = 0. \tag{7}$$

The presence of the photoelectron current implies the deputy is in the sunlight. When in the Earth's shadow, the current balance contains all of the same terms except for I_{ph}. A numerical root finder is used to solve for ϕ_D in Eq. 7.

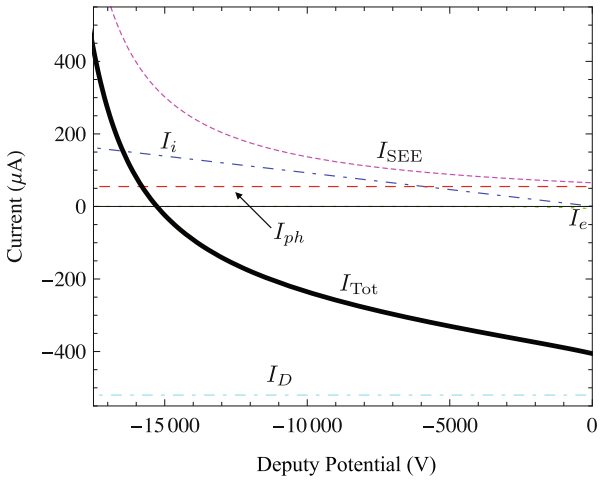

Fig. 2 Currents acting on the deputy for a range of deputy potentials. Deputy achieves a potential that results in I_{Tot}=0

An example charging scenario is presented in Fig. 2. Shown are the various currents impacting deputy charging for space weather conditions of $n_e = 0.9$ cm^{-3}, $n_i = 9.5$ cm^{-3}, $T_i = 50$ eV, and $T_e = 1250$ eV. These plasma parameters are representative of quiet conditions in GEO (i.e. no solar storm activity) and correspond roughly to a 12 PM local solar time [11]. More details about the space weather environment may be found in the next section. The results assume a beam energy of E_{EB} =40 keV and a beam current of I_t=520 μA. The tug and deputy are treated as spheres, with radii of $r_T = 2$ m and $r_D = 0.935$ m. With these conditions, the tug achieves a potential of $\phi_T = 21.5$ kV and the deputy reaches a potential of $\phi_D = -15.3$ kV. As seen in Fig. 2, the deputy potential results in a net zero current balance, i.e. $I_{\text{Tot}} = 0$. While the plasma electron current is included in the current balance, for the deputy it provides an insignificant contribution to charging at the high potential levels achieved. The tug and deputy potentials as a function of beam current are shown in Fig. 3. The tug potential increases linearly with beam current, while the deputy potential has its largest value around $I_t = 350$ μA

There are two electron beam parameters that may be used to influence charging: the beam energy and potential. Generally, a higher beam energy will result in higher deputy charging. This is due to the reduced secondary electron emission that stems from the higher energy of the incoming beam electrons. As the energy of an absorbed electron increases, fewer secondary electrons are emitted. Because the secondary electrons essentially result in the loss of some fraction of the incoming beam current, reducing the number of secondary electrons emitted will improve deputy charging. Thus, the beam energy is treated as constant, while the beam current is considered to be a control variable. Depending on the space weather conditions, increasing or decreasing the beam current can improve or worsen deputy charging, as shown in Fig. 3. However, the tug will always charge to higher potentials as the beam current is increased, up to the level of the beam energy ($q\phi_T \leq E_{EB}$). Choosing a beam current

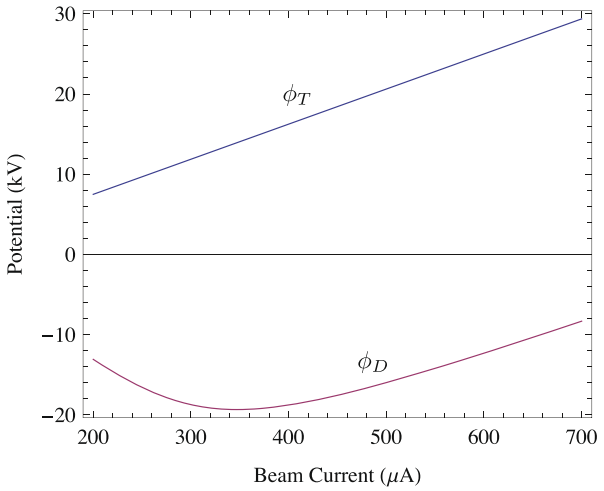

Fig. 3 Tug and deputy potentials as a function of beam current

to maximize the resulting electrostatic force requires a careful balance between tug and deputy charging, as well as consideration of changes in space weather. Increasing the current will increase the tug potential, but beyond a certain point higher current starts to reduce the deputy potential (magnitude). The resulting electrostatic force is a function of both the tug and deputy potentials. Thus, improvements to the electrostatic force resulting from increases in the tug potential can be offset by the corresponding decrease in deputy potential that comes from increasing beam current levels.

There is an inherent assumption in the electrostatic tractor concept that debris objects will be able to accept and distribute charge. Due to the potential impacts of spacecraft charging on operations and spacecraft lifetime, much work has been performed in this area [1, 6, 10, 13, 18, 21]. Typically, these studies focus on a single satellite in orbit and investigate natural charging events that occur as a result of the space weather environment. A serious concern for spacecraft that experience differential charging across their outer surface is electrostatic discharge (ESD) events, where arcing occurs between different substructures possessing a significant surface potential difference [18]. These ESD events can be destructive to electronic hardware. Recent studies indicate that large satellites in GEO may experience many thousands of discharges over their lifetimes [6]. With the electrostatic tug concept, the electron beam is used to raise the absolute potential of the vehicle, and thus avoids the differential charging issues. Current GEO spacecraft construction practice ensures that all outer surfaces are interconnected to a common ground, thus minimizing differential charging issues [24]. This also has the benefit of helping to distribute charge over a deputy structure, which improves electrostatic tractor performance. For electrostatic tugging, potential levels on the order of tens of kiloVolts are required [26]. While certainly the near proximity of highly charged spacecraft raises a concern of potential arcing between tug and debris, in GEO arcing occurs over distances of a few centimeters for kiloVolt levels of potential difference [5]. This is many times smaller than the separation distances considered, so arcing between tug and debris is not a concern.

Space Weather Environment at GEO

The charging results are dependent on the local space weather environment at GEO. The plasma density and temperature varies considerably, both with solar activity and local time. To provide a realistic model for the GEO environment, the ten year averaged measurements presented in [11] are used. The data were collected over an eleven year period from 1990-2001 and cover roughly one complete solar cycle. In this paper, we seek to characterize the impacts of changes in space weather that occur over an average day during quiet solar conditions. While extreme geomagnetic storms do create periods of highly perturbed space weather conditions, these do not make up a significant portion of the time required for an electrostatic tugging maneuver (several months). Thus, a model for the variations in space weather throughout a single GEO orbit is sought for a K_p index of 1.5. The K_p index is a measure of solar activity, and a value of 1.5 represents a condition of low solar activity.

In the GEO environment, there are two populations of ions: hot and cold. The hot ions generally have temperatures in the 10 keV range, with densities on the order

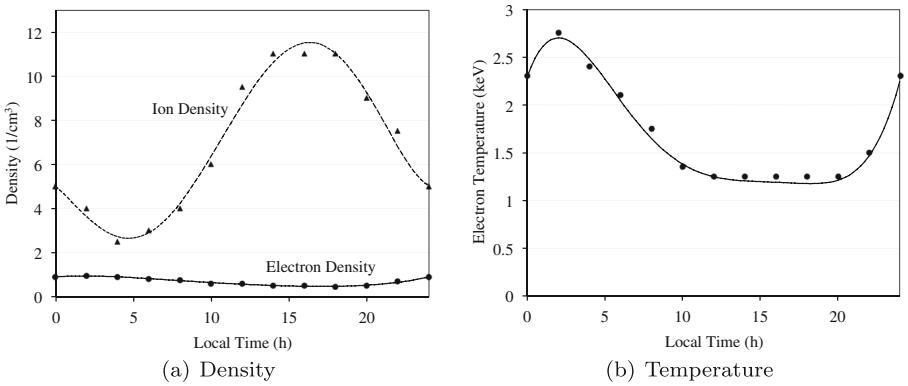

Fig. 4 GEO space weather parameters as a function of local time for $K_p = 1.5$. Markers represent data values taken from [11] and lines show polynomial data fits

of 1 cm^{-3}. The cold ions, which have their origins in the ionosphere, have temperatures between 3 and 100 eV and densities that range from less than 1 to over 10 cm^{-3}. These cold ions are most prevalent in the periods of low solar activity considered here. The ratio of hot to cold ion current collected by the spacecraft is roughly proportional to $T_{i,C}/T_{i,H}$, where the subscripts C and H denote cold and hot ions, respectively. Considering the temperature ranges for the hot and cold ion populations, the current due to the hot ions is around 1-5 % of that from the cold ions. Thus, in the charging computations throughout this study only the cold ion population will be used to compute the plasma ion currents as it predominates over the contributions from hot ions.

The data taken from [11] are presented in Fig. 4. To provide continuous functions for the various parameters, polynomial fits are used, and are chosen to provide

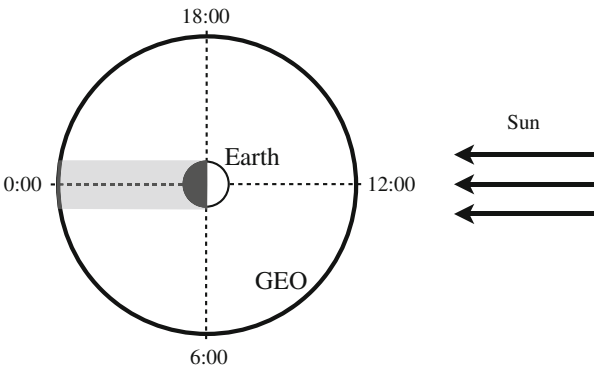

Fig. 5 Illustration of local time at GEO, looking down at the north pole. Shaded region represents Earth shadow period

continuity across midnight ($f(0) = f(24)$). The function used to fit each set of data values is

$$f(x) = \sum_{i=0}^{5} a_i x^i,$$

where x represents local time in hours, as illustrated in Fig. 5. The coefficients a_i for the electron density, electron temperature, and ion density are summarized in Table 1. Unfortunately, no data are available for the cold ion temperature variations as a function of local time, so a constant value of T_i =50 eV is used. The fit functions are plotted with their corresponding data sets in Fig. 4.

Space Weather Impacts on Tugging

Electrostatic Force Modeling

The electrostatic tugging is accomplished using the attractive electrostatic force generated between the tug and deputy. In this section, the procedure for computation of this electrostatic force is explained. Throughout the following developments, it is assumed that the tug and deputy are both spherical, with radii of r_T and r_D. In the space weather environment with the electron beam properly focused, the tug and deputy will achieve voltages of ϕ_T and ϕ_D, respectively. In order to compute the resulting electrostatic force, the charges on tug and deputy are required. Here, a position dependent capacitance model is used [25, 31, 32]. The voltage and charges on the tug and deputy are related through

$$\begin{bmatrix} \phi_T \\ \phi_D \end{bmatrix} = k_c \begin{bmatrix} \frac{1}{r_T} & \frac{1}{\rho} \\ \frac{1}{\rho} & \frac{1}{r_D} \end{bmatrix} \begin{bmatrix} q_T \\ q_D \end{bmatrix}, \tag{8}$$

where ρ is the separation distance between tug and deputy, $k_c = 8.99 \times 10^9$ Nm^2/C^2 is Coulomb's constant, and q_T and q_D are the charges on tug and deputy, respectively.

Once ϕ_D and ϕ_T are computed using the current balances detailed above, Eq. 8 is inverted to solve for the charges. These charges are then inserted into the electrostatic force equation

$$F_e = k_c \frac{q_T q_D}{\rho^2}. \tag{9}$$

Table 1 Coefficients used to fit space weather data

Parameter	a_5	a_4	a_3	a_2	a_1	a_0
n_e	9.447e-7	−5.601e-5	1.425e-3	0.0170	0.04804	0.9
n_i	4.144e-5	−2.270e-3	.03558	−.09276	−0.6345	5.0
T_e	1.112e-5	−6.948e-4	0.01599	−.1564	.4568	2.30

This force acts equally and opposite on the tug and deputy, and its direction is dependent on the relative orientation between the two objects. A positive value signifies a repulsive force, while a negative value represents an attractive force.

Due to the space weather environment, some shielding of this electrostatic force will occur. The distance over which this shielding is prevalent is described by the Debye length of the local plasma [2]. The space weather conditions considered in this study yield Debye lengths that are on the order of tens of meters. However, because of the high potential levels obtained by tug and deputy, the Debye shielding effect will be several times smaller than predicted by the standard Debye length calculation. As discussed in [22] and [35], objects charged to tens of kiloVolts in the space environment experience effective Debye lengths several times larger. Looking specifically at this phenomenon as it pertains to charging in quiet GEO space weather conditions, the effective Debye lengths are predicted to be roughly five times larger than the classic Debye shielding model predicts [35]. For the space weather conditions in Fig. 4, the classic Debye lengths range from 15-35 meters, leading to effective Debye lengths over 75 meters. This means that the space weather environment will not contribute significant shielding of the electrostatic force below distances of 75 meters. Because the separation distances considered here are less than 20 meters, the impacts of Debye shielding are insignificant and will not be included in the force model.

Beam Current Selection

The electron beam is what drives the charging of both the tug and deputy. The beam current and energy are each factors that contribute the resulting potentials achieved by the tug and deputy. Here we will treat the beam energy as a constant, with a value of E_{EB} =40 keV. With a constant beam energy, beam current control is considered as the primary method for electrostatic force manipulation. Two different scenarios are considered: constant beam current and varied beam current. The constant beam current scenario is straightforward; a particular current value is chosen and maintained throughout the duration of the tugging. A variable current, on the other hand, requires an analysis of the space weather environment fluctuations over a typical day to help choose an appropriate current profile.

The magnitude of the electrostatic force between deputy and tug is directly responsible for the rate at which reorbiting occurs. A larger force will yield a faster reorbiting time, and so a method for maximizing this force using beam current control is desired. In this study, an open-loop current control strategy as a function of local time is used, which assumes known nominal GEO space weather variations. The following results assume a beam energy of 40 keV, a tug-deputy separation distance of 12.5 m, a tug radius of two meters, and a deputy radius of 0.935 meters. The deputy radius is chosen to provide an equivalent surface area to the cylindrical deputy model used in the numerical simulation later in the paper. To determine the optimal current, the $FindMinimum$ numerical minimization tool in Mathematica is used. Using the electrostatic tractor force expression in Eq. 9 as the function to be minimized, the optimal current which will yield the largest electrostatic force for a given local time is computed. Note that Eq. 9 will always be negative due to the opposite polarities of

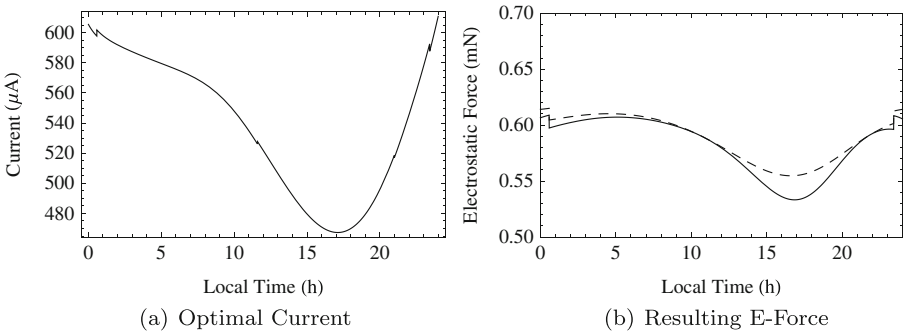

(a) Optimal Current (b) Resulting E-Force

Fig. 6 **a** Optimal electron beam current as a function of local time and **b**) electrostatic force resulting from optimal beam current (*dashed*) and constant current of 540 μA (*solid*). The results shown assume $E_{EB} = 40keV$, $r_T = 2$ m, and $r_D = 0.935$ m

the charges q_T and q_D. The optimal current history is shown in Fig. 6a, and the resulting electrostatic force in Fig. 6b. The discontinuities on either side of midnight are due to the lack of photoelectron emission by the deputy while in the earth's shadow.

The maximum beam current occurs at midnight, while the minimum occurs around 17:00. To explain this trend requires an examination of the tug and deputy potentials as a function of beam current and local time. Figure 7 shows these potentials for a range of currents between 300 and 700 μA. If a fixed current is held throughout the day, the tug will experience its maximum potential around dusk. This is due to the trend in electron density. As the electron density decreases after noon, there is less electron current returning to the tug for a given potential. In order to balance electron beam emission with the plasma electron current, the tug must settle to a higher potential.

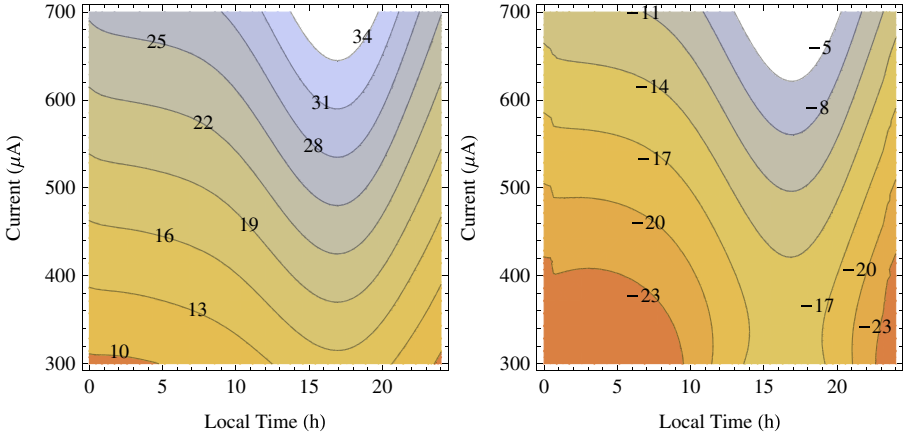

(a) ϕ_T (kV) (b) ϕ_D (kV)

Fig. 7 Potentials achieved by tug and deputy as a function of local time for a range of currents. The results shown assume $E_{EB} = 40keV$, $r_T = 2$ m, and $r_D = 0.935$ m

The deputy, on the other hand, experiences its minimum potential at the same time that the tug experiences its maximum. A casual study of the space weather trends would suggest that this is due to increasing ion density after noon. While this trend does contribute partially to the decrease in deputy potential, the primary factor in this reduction is the secondary electron emission generated by the incoming electron beam current. The amount of secondary electrons emitted due to an incoming electron is a function of the incoming electron's energy. The maximum secondary electron yield occurs when the energy of an incoming electron is equal to $E_{max} = 300$ eV in the model implemented here. As the energy of an incoming electron increases, the corresponding secondary electron yield is reduced. The energy of the incoming electrons from the electron beam is equal to the beam energy minus the potential difference between tug and deputy, i.e. $E_{eff} = E_{EB} - q\phi_T + q\phi_D$. As the tug potential ϕ_T increases after noon due to lower electron density, the energy of the incoming beam electrons is reduced considerably. These lower energy electrons, in turn, result in a higher secondary electron current that reduces the deputy potential.

It is also at this dusk period where the difference in the magnitudes of tug and deputy potentials is at its greatest point. There is an ideal potential difference between tug and deputy that will yield the maximum electrostatic force. In [29], expressions for these ideal potentials in a vacuum are derived as

$$\phi_T = \frac{E_{EB}}{2}\frac{\rho^2 - 2\rho r_D + r_T r_D}{(\rho - r_T)(\rho - r_D)} \tag{10a}$$

$$\phi_D = \frac{E_{EB}}{2}\frac{\rho^2 - 2\rho r_T + r_T r_D}{(\rho - r_T)(\rho - r_D)}. \tag{10b}$$

These relationships assume that the potential difference between tug and deputy is equal to the electron beam energy ($E_{EB} = q\phi_T - q\phi_D$). In reality, this will never be the case because the various currents that contribute to the charging process cause some losses in efficiency. Still, this ideal potential split provides a baseline for analyzing the reasons why the minimum forces occur when they do. Using Eq. 10 yields

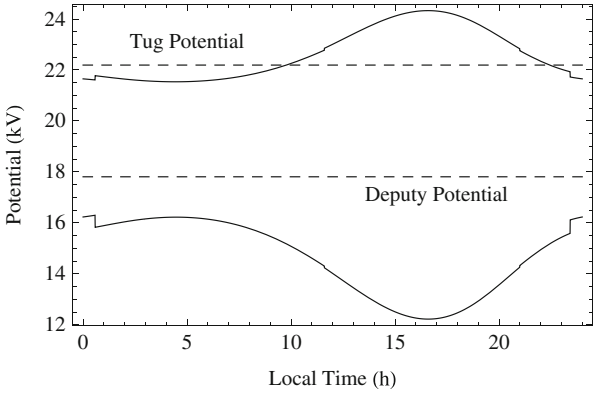

Fig. 8 Potential magnitudes of tug and deputy that result from applying ideal current history. Dashed lines represent ideal potentials computed assuming $E_{EB} = q\phi_T - q\phi_D$

ideal potentials of ϕ_T =22.2 kV and ϕ_D =-17.8 kV. The magnitudes of the actual potentials achieved using the ideal current history are shown in Fig. 8, along with the values computed from Eq. 10. The deputy potential is always smaller than its ideal value, which reflects the losses due to the charging process. Note that the maximum electrostatic force occurs when the potential split best approximates the ideal value. Reducing the beam current during the post-noon timeframe is necessary for limiting the increase in the difference between tug and deputy potentials. Without reducing the current, the tug potential would climb higher and the deputy potential would descend lower, further deviating from the ideal split. This explains why the ideal current history follows the trend in Fig. 6a.

We now turn our attention to the case of maintaing a constant electron beam current throughout the duration of the orbit. Choosing an ideal current history is dependent on knowledge of the space weather environment, and such information may not be available in real time. A much simpler approach would be to simply hold a fixed beam current. Of course, there will be some reduction in the magnitude of the electrostatic forces, which may or may not be significant enough to severely impact performance of the tugging process. Instead of varying the current with local time, a fixed current of 540 μA is used. The resulting electrostatic forces are shown in Fig. 6b. Comparing with the results from the ideal current history, the largest reduction in electrostatic force occurs during the dusk period discussed previously. Again, maintaining a constant current results in an increase in tug potential and decrease in deputy potential during this period that leads to a weaker electrostatic force. Even at the worst point, the reduction in electrostatic force is no more than about 5 %.

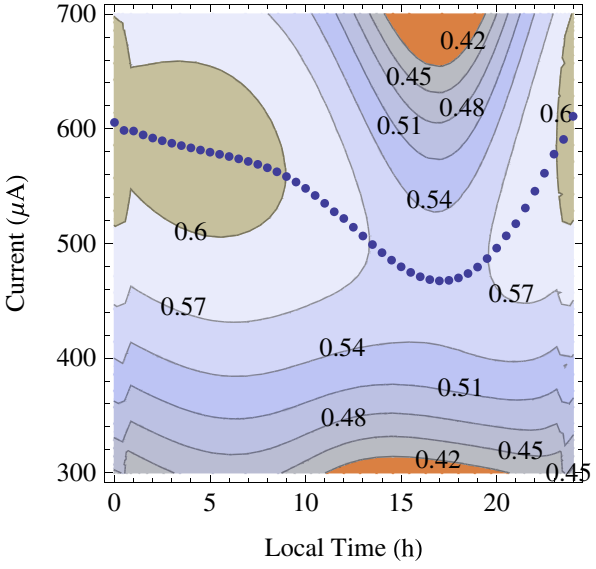

Fig. 9 Electrostatic forces (in mN) computed for a variety of electron beam current values as a function of local time. Data points illustrate the ideal current history

To illustrate why the losses are small, a plot of the electrostatic force as a function of local time and current is presented in Fig. 9. Also plotted is the ideal current history. The regions around the ideal current values are relatively flat, featuring shallow force dropoffs. While the ideal current varies by 140 μA throughout the course of a day, losses of no more than 5 % can be achieved by maintaining a constant current of anywhere between 400 and 550 μA. Again, this raises the question of whether or not the added complexity required to predict an ideal current as a function of space weather is worth it when very similar performance can be obtained by simply maintaining a fixed current with a large margin of error.

Relative Motion Control

To model the relative motion of the tug with respect to the deputy, the sigma-set relative motion description is used [16]. The sigma-set description is developed from the Clohessy-Wiltshire (CW) equations [7, 27], and uses three coordinates to describe relative orbital motion. While the CW equations could be used to model the relative motion, for the electrostatic tugging application it is attractive to use coordinates which contain the separation distance due to its direct influence on the electrostatic forces that heavily impact the relative motion. In prior work, a spherical coordinate description is used for this reason [15]. However, for certain relative orientations of tug and deputy, this spherical coordinate description is singular. The sigma-set relative motion description was developed as an alternative that allows for the use of separation distance directly as a coordinate while avoiding such singularities.

Assuming the deputy craft is at the origin of the Hill-frame and denoting the CW coordinates of the tug as x, y, and z, the sigma-set consists of three parameters defined by

$$L = \pm\sqrt{x^2 + y^2 + z^2} \tag{11a}$$

$$\sigma_1 = \frac{y}{x + L} \tag{11b}$$

$$\sigma_2 = \frac{z}{x + L}. \tag{11c}$$

The presence of the $\pm$ in L results in two different values for the sigma-set that describe the same relative position. It is this non-uniqueness that allows for singularity avoidance. When $x = -L$, both σ_1 and σ_2 will be infinite. However, a switch to the shadow set may be performed ($L_s = -L$, $\sigma_{1,s} = -\sigma_1/\sigma^2$, $\sigma_{2,s} = -\sigma_2/\sigma^2$) at any time to prevent approaching this singularity. While the original set is ill-defined when $x = -L$, its shadow set is well defined. In this paper, the standard of switching between original and shadow set when $\sigma^2 > 1$ is used. Further details regarding the shadow set switching may be found in [16].

The dynamics of the sigma-set are described by

$$\begin{bmatrix} \ddot{L} \\ \ddot{\sigma}_1 \\ \ddot{\sigma}_2 \end{bmatrix} = \begin{bmatrix} h_L \\ h_{\sigma_1} \\ h_{\sigma_2} \end{bmatrix} + [G_\sigma]^{\mathcal{H}}\boldsymbol{u}, \tag{12}$$

where

$$\begin{aligned} h_L &= \frac{L}{\left(1+\sigma^2\right)^2}[3n^2(\sigma_1^4+\sigma_2^4+1)+4\dot{\sigma}_1 n-2n\sigma_2^2(5n+2\dot{\sigma}_1) \\ &\quad +2n\sigma_1^2(3n(-1+\sigma_2^2)+2\dot{\sigma}_1)+8n\sigma_1\sigma_2\dot{\sigma}_2+4\dot{\boldsymbol{\sigma}}^T\dot{\boldsymbol{\sigma}}] \\ h_{\sigma_1} &= -\frac{1}{2L\left(1+\sigma^2\right)}[-6n^2L\sigma_1^3+2n\sigma_1^4\dot{L}+4\sigma_1^2\dot{L}\left(n+\dot{\sigma}_1\right) \\ &\quad -\left(1+\sigma_2^2\right)\dot{L}\left(2n\sigma_2^2-2\left(n+2\dot{\sigma}_1\right)\right)-8L\sigma_2\left(n+\dot{\sigma}_1\right)\dot{\sigma}_2 \\ &\quad +2L\sigma_1\left(3n^2-5n^2\sigma_2^2-2\dot{\sigma}_1^2+2\dot{\sigma}_2^2\right)] \\ h_{\sigma_2} &= \frac{1}{2L\left(1+\sigma^2\right)}[-4n\sigma_1^3\sigma_2\dot{L}-4n\sigma_1\left(\sigma_2+\sigma_2^3\right)\dot{L}-4\dot{L}\dot{\sigma}_2+8L\sigma_1\dot{\sigma}_1\dot{\sigma}_2 \\ &\quad +2\sigma_1^2\left(2n^2L\sigma_2-2\dot{L}\dot{\sigma}_2\right)-\sigma_2\left(4\sigma_2\dot{L}\dot{\sigma}_2+4L\left(2n^2\left(1-\sigma_2^2\right)\right.\right. \\ &\quad \left.\left.+\ 2n\dot{\sigma}_1+\dot{\sigma}_1^2-\dot{\sigma}_2^2\right)\right)] \end{aligned} \tag{13}$$

and

$$\begin{aligned} [G_\sigma] &= \begin{bmatrix} \frac{1-\sigma^2}{1+\sigma^2} & \frac{2\sigma_1}{1+\sigma^2} & \frac{2\sigma_2}{1+\sigma^2} \\ -\frac{\sigma_1}{L} & \frac{1-\sigma_1^2+\sigma_2^2}{2L} & -\frac{\sigma_1\sigma_2}{L} \\ -\frac{\sigma_2}{L} & -\frac{\sigma_1\sigma_2}{L} & \frac{1+\sigma_1^2-\sigma_2^2}{2L} \end{bmatrix} \\ {}^{\mathcal{H}}\boldsymbol{u} &= \begin{bmatrix} u_x \\ u_y \\ u_z \end{bmatrix}. \end{aligned} \tag{14}$$

Note that $\sigma^2 = \sigma_1^2+\sigma_2^2$, $\boldsymbol{\sigma} = [\sigma_1\ \sigma_2]^T$, and u_x, u_y, and u_z are the control accelerations of the tug in the Hill-frame. These control accelerations consist of both the thrusters employed by the tug and the electrostatic forces acting between tug and deputy.

In the equations of motion, n represents the mean motion of the deputy object. Because the sigma-set dynamics are derived from the CW equations, it is inherently assumed that n is constant. However, as the deputy object is towed this will no longer be the case. This issue is analyzed in [15]; because the electrostatic forces are small (on the order of mN), neglecting the mean motion rate of change does not introduce significant errors into the linearized CW equations. To account for the fact that the mean motion does change with time, n is simply replaced with the time-dependent $n(t)$. Thus, in the sigma-set equations of motion presented above, n is used to represent the time-varying mean motion of the deputy.

To develop a relative motion control law, the sigma-set error measure

$$\delta\boldsymbol{\zeta} = \boldsymbol{\zeta} - \boldsymbol{\zeta}_r = \begin{bmatrix} L \\ \boldsymbol{\sigma} \end{bmatrix} - \begin{bmatrix} L_r \\ \boldsymbol{\sigma}_r \end{bmatrix}. \tag{15}$$

is used. The subscript r denotes reference values that represent the desired relative position of tug with respect to deputy. By choosing the control acceleration as

$${}^{\mathcal{H}}\boldsymbol{u} = [G_\sigma]^{-1}\left(-[K]\delta\boldsymbol{\zeta} - [P]\delta\dot{\boldsymbol{\zeta}} - \begin{bmatrix} h_L \\ h_{\sigma_1} \\ h_{\sigma_2} \end{bmatrix} + \ddot{\boldsymbol{\zeta}}_r\right), \tag{16}$$

asymptotic tracking of a possibly time-varying reference relative motion trajectory $(L_r, \boldsymbol{\sigma}_r)$ is guaranteed, where $[K]$ and $[P]$ are positive definite gain matrices.[16] The control acceleration contains contributions from the electrostatic force and tug thrusters, expressed as

$${}^{\mathcal{H}}\boldsymbol{u} = {}^{\mathcal{H}}\boldsymbol{F}_e\left(\frac{1}{m_T} + \frac{1}{m_D}\right) + \frac{{}^{\mathcal{H}}\boldsymbol{T}_t}{m_T}, \tag{17}$$

where ${}^{\mathcal{H}}\boldsymbol{F}_e$ is the electrostatic force acting on the tug in Hill-frame components, ${}^{\mathcal{H}}\boldsymbol{T}_t$ is the tug thrust force in Hill-frame components, m_T is the tug mass, and m_D is the deputy mass.

The electron beam is used to affect the tug and deputy charging, which will generate the electrostatic force ${}^{\mathcal{H}}\boldsymbol{F}_e$. The thrusting must compensate for this electrostatic force to generate the required control acceleration ${}^{\mathcal{H}}\boldsymbol{u}$. The commanded thrust, then, is computed as

$${}^{\mathcal{H}}\boldsymbol{T}_t = m_T\left[{}^{\mathcal{H}}\boldsymbol{u} - {}^{\mathcal{H}}\boldsymbol{F}_e\left(\frac{1}{m_T} + \frac{1}{m_D}\right)\right]. \tag{18}$$

In order to estimate the electrostatic force for the feedforward compensation of ${}^{\mathcal{H}}\boldsymbol{F}_e$, some estimate of the charging on tug and deputy is required. Practically this can be challenging, as uncertainties in space weather conditions, craft geometries, and charging properties will result in differences between estimated values and the truth.

The impacts of improperly modeled electrostatic forces on relative motion are examined in [15]. Because the electrostatic force is directed along the line of sight from tug to deputy, it primarily affects the separation distance. If the electrostatic force is over-predicted, the tug will settle at a larger separation distance than desired ($|L| > |L_r|$). If the electrostatic force is under-predicted, two different responses are possible. If the magnitude of under-prediction is small enough, the tug will settle to a closer separation distance than desired ($|L| < |L_r|$). If the under-prediction is severe enough, the controller will not provide enough thrust to prevent a collision between tug and deputy. Clearly, such a collision is undesirable and should be avoided at all costs. Different factors influence the allowable level of under-prediction before collision occurs, including the desired separation distance L_r, the tug and deputy masses, and the control gains [15]. If the gain matrices $[P]$ and $[K]$ are chosen to be diagonal,

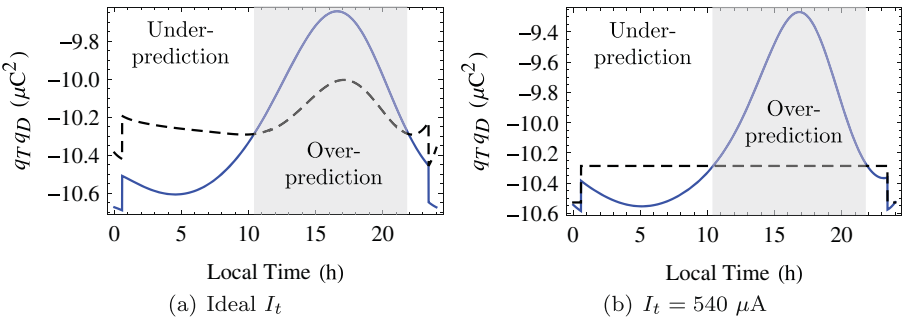

Fig. 10 Charge product $q_T q_D$ for **a**) ideal beam current history and **b**) constant beam current of 540 μA. *Solid lines* represent true charge product, while *dashed lines* represent estimated values

the equations of motion decouple. With an improperly modeled electrostatic force, the dynamics of L are described by

$$\ddot{L} + P_L \dot{L} + K_L(L - L_r) = \frac{k_c}{L^2}(q_T q_D - q_{T,e} q_{D,e}) \left(\frac{1}{m_T} + \frac{1}{m_D} \right), \tag{19}$$

where $q_{T,e}$ and $q_{D,e}$ are the estimated charges on tug and deputy. Charge over-prediction corresponds to $|q_T q_D| < |q_{T,e} q_{D,e}|$, while charge under-prediction is defined as $|q_T q_D| > |q_{T,e} q_{D,e}|$. Note that while [15] parameterizes the relative motion using spherical coordinates, the closed loop dynamics for L are equivalent to Eq. 19. If an estimate of the maximum level of under-prediction is available, a collision may be avoided by ensuring that [15]

$$K_L \geq \frac{27 \mu \Delta Q_{\max}}{4 L_r^3}, \tag{20}$$

where $\mu = k_c \left(\frac{1}{m_T} + \frac{1}{m_D} \right)$ and $\Delta Q_{\max} = \max(|q_T q_D - q_{T,e} q_{D,e}|)$.

To determine the lower limit for K_L, we consider the impacts of changing space weather conditions on charge prediction. Because space weather conditions are dynamic and may be difficult to incorporate into a realtime estimate, constant average values are used for charge prediction. Considering the expected parameter ranges shown in Fig. 4, values of $n_i = 7$ cm^{-3}, $T_i = 50$ eV, $n_e = 0.7$ cm^{-3}, and $T_e = 1.7$ keV are used in the charging model to estimate the charges on tug and deputy. The resulting true and estimated charge products as a function of local time are shown in Fig. 10, assuming $r_T = 2$ m and $r_D = 0.935$ m. Results are computed using both the ideal beam current history and a constant beam current of 540 μA. There is a roughly even split in the amount of time that is spent in under-prediction versus time spent in over-prediction. During periods of over-prediction, some performance loss occurs because of the smaller electrostatic force that results from a larger separation distance. This is somewhat balanced by the increased performance obtained during under-prediction when the tug and deputy are closer than desired.

The difference between true and estimated charge products is used to bound K_L. For the ideal current history, the max under-prediction occurs just before 4:00 with a $\Delta Q_{\max} = 0.35$ μC^2. For constant current of 540 μA, the worst under-prediction

occurs just after 5:00 with a $\Delta Q_{\max} = 0.21\ \mu C^2$. The tug and deputy masses are required for evaluation of Eq. 20; values of $m_T = 500$ kg and $m_D = 1000$ kg are used here and in the following numerical simulation. Using the higher value of $\Delta Q_{\max} = 0.35\ \mu C^2$, the lower limit of K_L is found to be $K_L = 3.26 \times 10^{-8}\ s^{-2}$.

For the debris reorbiting scenario considered in this study, slight errors between the true and desired separation distance are not a serious concern. The ultimate goal is raising a debris object into a graveyard orbit [17], and taking slightly more or less time to get there is not a major obstacle to achieving this goal. If more precision is required during a deputy reorbiting maneuver, these slight errors could have a significant impact and would need to be considered.

Numerical Simulation

The spacecraft charging model is implemented into a full numerical simulation and used to model relative motion while performing charge transfer and electrostatic tugging. A total simulation period of two days is used, and both the ideal current history and a constant beam current of 540 μA are applied. The initial orbital elements for both tug and deputy are summarized in Table 2. In the debris reorbiting scenario modeled here, the tug maintains a constant position 12.5 meters ahead of the deputy in the along track direction, which corresponds to reference sigma-set values of $L_r = 12.5,\ \sigma_{1r} = 1,\ \sigma_{2r} = 0$ (shadow set values of $L_{rs} = -12.5,\ \sigma_{1rs} = -1,\ \sigma_{2rs} = 0$). The control gains used are $[K] = 3.75 \times 10^{-7}[I_{3\times3}]\ s^{-2}$ and $[P] = 1.13 \times 10^{-3}[I_{3\times3}]\ s^{-1}$. Note that the values K_i are an order of magnitude larger than the lower limit required to avoid collision, and the gains will result in a settling time of 2.4 hours.

Multi-Sphere Model of the Deputy

The tug is modeled using a sphere with a radius of two meters. Rather than treating the deputy object as spherical, a cylindrical model is used instead. This results in off-axis forces that are no longer necessarily aligned with the line of sight from tug to deputy. Furthermore, electrostatic torques affect the attitude motion of the deputy. As the deputy tumbles, even with a fixed separation distance between tug and deputy, the electrostatic force magnitude will no longer be constant. Incorporating a non-spherical model allows for inclusion of these effects, which in turn provides for a more realistic simulation of charged relative motion. In general, a debris object will be non-spherical and the electrostatic tugging process would experience these phenomena.

Table 2 Initial orbital elements of tug and deputy

	a (km)	e	i (°)	Ω (°)	ω (°)	ν (°)
Deputy	42164	0	0	0	0	0
Tug	42164.075	1e-6	-0.001	0	0	1e-5

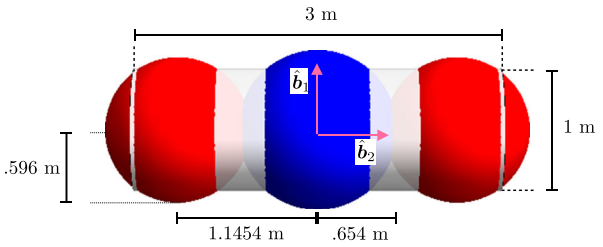

Fig. 11 Multi-sphere model used to represent the 3x1 meter cylindrical deputy object

The multi-sphere method (MSM) is used to compute the electrostatic forces and torques between tug and deputy [33]. The deputy is modeled as a cylinder with a diameter of one meter and a height of three meters. To compute the charge on the deputy an approximation of three spheres is used, as depicted in Fig. 11. In the deputy body frame $\mathcal{B} : \{\hat{\boldsymbol{b}}_1,\ \hat{\boldsymbol{b}}_2,\ \hat{\boldsymbol{b}}_3\}$ each sphere is located at a position of $\boldsymbol{r}_i$ and has an associated radius of R_i. The sphere locations and radii are presented in Table 3.

The procedure for computing the electrostatic forces and torques between tug and deputy follows. First, the potentials on tug and deputy are computed using the charge model detailed above. Each sphere on the deputy is assumed to have the same potential of ϕ_D. Denoting the charge on each individual sphere as q_i, the matrices $\boldsymbol{\Phi} = [\phi_D\ \phi_D\ \phi_D\ \phi_T]^T$ and $\boldsymbol{q} = [q_1\ q_2\ q_3\ q_T]^T$ are constructed. Using the position dependent capacitance model, the potentials and charges are related through

$$\boldsymbol{\Phi} = k_c[C_M]^{-1}\boldsymbol{q}. \tag{21}$$

The inverse of the position dependent capacitance matrix, $[C_M]^{-1}$, is then expanded as

$$[C_M]^{-1} = \begin{bmatrix} 1/R_1 & 1/r_{1,2} & 1/r_{1,3} & 1/r_{1,T} \\ 1/r_{2,1} & 1/R_2 & 1/r_{2,3} & 1/r_{2,T} \\ 1/r_{3,1} & 1/r_{3,2} & 1/R_3 & 1/r_{3,T} \\ 1/r_{T,1} & 1/r_{T,2} & 1/r_{T,3} & 1/r_T, \end{bmatrix}. \tag{22}$$

where $r_{i,j}$ is the distance between spheres i and j. The subscript T refers to the tug, so that $r_{1,T}$ is the separation distance between deputy MSM sphere 1 and the tug. To solve for the charges, $\boldsymbol{q}$, Eq. 21 is inverted. The total electrostatic force acting on the deputy is obtained by summing up the forces on the individual MSM spheres, i.e.

$$\boldsymbol{F}_{e,D} = -k_c q_T \sum_{i=1}^{3} \frac{q_i}{r_{i,T}^3}\boldsymbol{r}_{i,T}, \tag{23}$$

Table 3 Radii and body-frame sphere locations used to represent cylinder in MSM model

Sphere	Body Frame Location $\boldsymbol{r}_i$ (m)	Sphere Radius R_i (m)
1	$-1.454\hat{\boldsymbol{b}}_2$	.5959
2	$\boldsymbol{0}$	.6543
3	$1.454\hat{\boldsymbol{b}}_2$	.5959

where $\boldsymbol{r}_{i,T}$ is the vector from MSM sphere i to the tug. This force acts equal and opposite on the tug, so that $\boldsymbol{F}_{e,T} = -\boldsymbol{F}_{e,D}$. The total torque acting on the deputy resulting from the electrostatic interaction with the tug is computed as

$$\boldsymbol{T}_e = -k_c q_T \sum_{i=1}^{3} \frac{q_i}{r_{i,T}^3} \boldsymbol{r}_i \times \boldsymbol{r}_{i,T}. \tag{24}$$

The spherical geometry of the tug prevents any electrostatic torques from acting on it.

Tug and Deputy Dynamics

To propagate the orbits of both tug and deputy, inertial two-body dynamics are used. In the case of the tug, the motion is governed by gravity, electrostatic forces, and thrusting. The tug trajectory is determined through integration of

$$\ddot{\boldsymbol{p}}_T = -\frac{\mu}{p_T^3} \boldsymbol{p}_T + \frac{\boldsymbol{F}_{e,T}}{m_T} + \frac{\boldsymbol{T}_T}{m_t}, \tag{25}$$

where $\boldsymbol{p}_T$ is the position of the tug in the earth centered inertial (ECI) frame. Similarly, the deputy orbit is propagated using

$$\ddot{\boldsymbol{p}}_D = -\frac{\mu}{p_D^3} \boldsymbol{p}_D + \frac{\boldsymbol{F}_{e,D}}{m_D}. \tag{26}$$

Local time is computed by assuming the sun direction is $\hat{\boldsymbol{r}}_\odot = [1\ 0\ 0]^T$ in the ECI frame. Equations 25 and 26 serve as the truth model for the tug and deputy orbital dynamics. They describe how the orbits of both objects evolve under the influence of gravity, thrusting, and electrostatic forces. For the tug thrust control ($\boldsymbol{T}_T$), Eqs. 16 and 18 are used, and the exact tug and deputy orbital positions (from Eqs. 25 and 26) are assumed to be known to the controller. The electrostatic force compensation in the controller is obtained using the averaged space weather values $n_i = 7\ \text{cm}^{-3}$, $T_i = 50$ eV, $n_e = 0.7\ \text{cm}^{-3}$, and $T_e = 1.7$ keV, and assumes the deputy is spherical with a radius of $r_D = 0.935$ m. The true electrostatic force used to propagate the orbits uses the MSM cylindrical model and the time-varying space weather conditions in Fig. 4.

The electrostatic forces and torques are a function of the deputy attitude, and so deputy attitude motion must be accounted for. Modified Rodrigues parameters ($\boldsymbol{\eta}$) are used to describe the deputy attitude, with the corresponding attitude dynamics [27]

$$\dot{\boldsymbol{\eta}} = \frac{1}{4}\left[(1-\eta^2)[I_{3\times 3}] + 2[\tilde{\boldsymbol{\eta}}] + 2\boldsymbol{\eta}\boldsymbol{\eta}^T\right]\boldsymbol{\omega} \tag{27a}$$

$$[J]\,\dot{\boldsymbol{\omega}} = -\boldsymbol{\omega} \times [J]\boldsymbol{\omega} + \boldsymbol{T}_e, \tag{27b}$$

where

$$[J] = \begin{bmatrix} 893.75 & 0 & 0 \\ 0 & 125.0 & 0 \\ 0 & 0 & 731.25 \end{bmatrix} \text{kg m}^2$$

is the deputy inertia tensor. The initial conditions used to propagate the deputy attitude are $\boldsymbol{\eta}_0 = \boldsymbol{0}$, $\boldsymbol{\omega}_0 = [1\ 2\ -0.6]^T$ (deg/s).

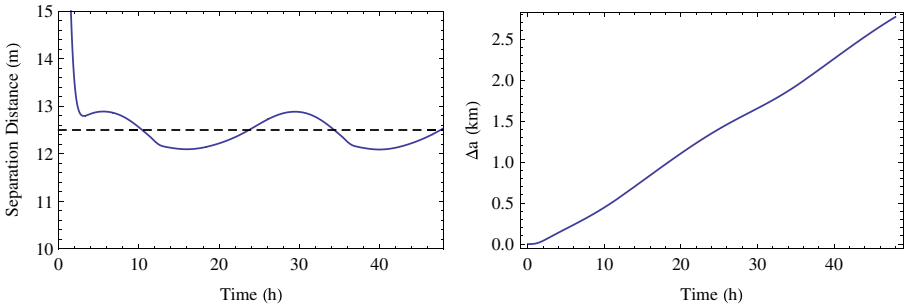

(a) Separation Distance (b) SMA Change

Fig. 12 **a** Separation distance between tug and deputy and **b** increase in deputy semimajor axis with application of ideal beam current history

Simulation Results

First, the effects of the ideal beam current history on relative motion and reorbiting are considered. After approximately 2.5 hours, the tug and deputy achieve the desired leader-follower alignment. The separation distance between tug and deputy throughout the duration of the simulation is presented in Fig. 12a. Though the desired separation distance is 12.5 meters, the actual separation oscillates about this value with a range of 0.8 meters. This results from the errors between the estimated and true electrostatic forces, and is expected. For the debris reorbiting scenario, these slight oscillations are of minor concern. The ultimate goal is merely increasing the semimajor axis of the deputy object to a high enough level to prevent reentry into GEO. Slight deviations from the desired performance do not hinder this goal.

The increase in deputy semimajor axis during the maneuver is shown in Fig. 12b. After two days, the deputy semimajor axis is about 2.6 kilometers larger than at the beginning of the maneuver. This agrees with earlier work predicting reorbiting performance using the electrostatic tug for debris mitigation applications, where semimajor axis corrections of 1-3 km per day are expected [14, 28]. There are slight variations in the rate of change of the semimajor axis, and these correspond with the periods of charge over- and under-prediction. Charge over-prediction occurs during the time of day when the electrostatic forces are at their smallest, and separation distances are at their largest. As a result, there is a weaker tug force pulling on the deputy, resulting in a slower increase in semimajor axis. The opposite occurs during the periods of under-prediction.

Next, attention is paid to application of a constant beam current of 540 μA throughout the maneuver. The separation distance history is very similar to what is depicted in Fig. 12a, and is not shown here for the sake of brevity. The same oscillations occur, with periods of smaller and larger separation distances than desired. To assess the performance differences between the constant beam current and ideal beam current histories, the resulting semimajor axis changes are compared. The difference between the deputy semimajor axis during the ideal and constant current

cases is shown in Fig. 13a. Positive values indicate that the ideal beam current history has achieved a larger semimajor axis increase than the constant beam current. A positive slope indicates that using the ideal current history is increasing the semimajor more quickly, while a negative slope implies that the constant beam current is increasing the semimajor axis more quickly. After 48 hours, charge control using the ideal beam history results in an additional 25 meter increase in the semimajor axis as compared to maintaining a constant beam current of 540 μA. This means that using the constant beam current would result in a performance loss on the order of 1%. This again raises the question of whether or not the performance benefits resulting from the optimized electrostatic force are worth the added complexity as compared to simply maintaining a constant beam current that works well for the expected range of nominal space weather conditions.

The ideal beam current history should result in larger electrostatic forces throughout the maneuver, which implies that the rate of semimajor axis change will always be larger than for the fixed current case. However, as seen in Fig. 13a, this is not the case. There are periods where the fixed beam current actually outperforms the ideal beam current case. Figure 13b shows the electrostatic forces resulting from both current histories. At certain times, the constant 540 μA current produces a larger electrostatic force than the ideal beam current. A few factors contribute to this result. First, the ideal beam current is computed assuming a spherical deputy geometry. The true physical model implemented in the numerical simulation is cylindrical, and this changes the current balance affecting the deputy potential. Specifically, the photoelectron current will not be equivalent between cylinder and sphere, and for the cylinder is dependent on the orientation of the deputy relative to the sun. Secondly, the differences in force estimation between the two cases result in slightly different separation distance histories. There are times when the constant current results in a closer separation distance than the ideal beam current. Because the voltages achieved in both cases are similar, the smaller separation distances yield larger forces for the constant current. These periods are brief, and generally the ideal beam current history does result in better performance. The widths of the electrostatic force curves in

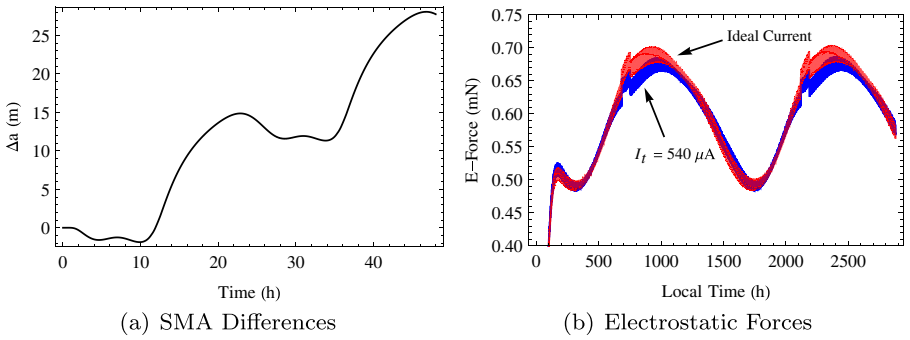

Fig. 13 **a** Difference in deputy semimajor axis evolution and **b** electrostatic force magnitudes resulting from application of ideal beam current history and a constant beam current of 540 μA

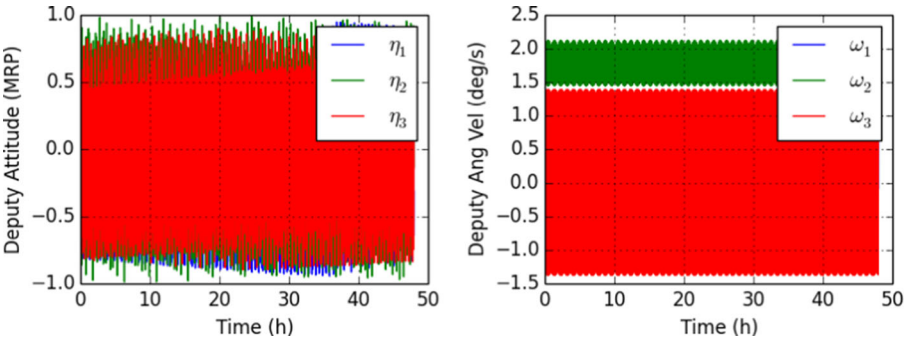

(a) Attitude (b) Angular Velocity

Fig. 14 Deputy attitude and angular velocity during maneuver for ideal beam current case

Fig. 13b are due to the deputy tumbling. Small oscillations occur in the electrostatic force magnitude due to this attitude motion. Plots of the deputy attitude history and angular velocity for the ideal beam current case are shown in Fig. 14.

Conclusions

In this paper, application of the electrostatic tractor concept for reorbiting a GEO debris object is considered. An electron beam is used to perform charge control of the tug and deputy craft, and a full charging model incorporating various current sources is used to compute the potentials on the two objects. Nominal GEO space weather conditions typical of low solar activity are used in the charging model. Two scenarios are considered for charge beam control: modifying the beam current to account for space weather variations in an attempt to maximize the electrostatic force and maintaining a constant beam current. Developing an ideal current model is dependent on a-priori knowledge of the space weather environment, and may be difficult or impractical in a real-time scenario. However, the analysis reveals that for typical space weather variations, similar performance can be obtained by simply maintaining a fixed current. This is promising for the electrostatic tractor concept, because it implies that knowledge of current space weather conditions is not a requirement for achieving acceptable performance. A numerical simulation is used to model the relative motion of tug and deputy, and fully incorporates the charge model and space weather variations. The relative control algorithm is used to maintain a leader-follower alignment of tug and deputy for the purposes of increasing the deputy semimajor axis. Differences between the estimated and true electrostatic forces lead to small oscillations about the desired separation distance. However, these small oscillations ($<$ 1 m) do not significantly hinder performance, and the electrostatic tractor achieves a semimajor axis increase of over one kilometer per day. With a target graveyard orbit of 300 km above GEO, this would require a total reorbiting time of 8-9 months.

References

1. Anderson P.C.: Characteristics of spacecraft charging in low earth orbit. J. Geophys. Res. Space Phys. **117**(A7), n/a–n/a (2012). doi:10.1029/2011JA016875
2. Bittencourt, J.: Fundamentals of Plasma Physics. Inc, Springer-Verlag New York (2004)
3. Bombardelli, C., Pelaez, J.: Ion beam shepherd for contactless space debris removal. AIAA J. Guid. Control. Dyn. **34**(3), 916–920 (2011). doi:10.2514/1.51832
4. Bombardelli, C., Urrutxua, H., Merino, M., Ahedo, E., Pelaez, J., Olympio, J.: Dynamics of ion-beam propelled space debris. In: International Symposium on Space Flight Dynamics. Sao Jose dos Campos, Brasil (2011)
5. Cho, M., Ramasamy, R., Matsumoto, T., Toyoda, K., Nozaki, Y., Takahashi, M.: Laboratory tests on 110-volt solar arrays in simulated geosynchronous orbit environment. J. Spacecr. Rocket. **40**(2), 211–220 (2003)
6. Cho, M., Sumida, T., Masui, H., Toyoda, K., Kim, J.H., Hatta, S., Wong, F., Hoang, B.: Spacecraft charging analysis of large geo satellites using muscat. IEEE Trans. Plasma Sci. **40**(4), 1248–1256 (2012). doi:10.1109/TPS.2012.2187074
7. Clohessy, W.H., Wiltshire, R.S.: Terminal guidance system for satellite rendezvous. J. Aerospace Sci. **27**(9), 653–658 (1960)
8. Couzin, P., Teti, F., Rembala, R.: Active removal of large debris: Rendezvous and robotic capture issues. In: 2nd European Workshop on Active Debris Removal, paper No. 7.5, Paris (2013)
9. Couzin, P., Teti, F., Rembala, R.: Active removal of large debris: System approach of deorbiting concepts and technological issues. In: 6th European Conference on Space Debris, paper No. 6a.P-17, Darmstadt (2013)
10. DeForest, S.E.: Spacecraft charging at synchronous orbit. J. Geophys. Res. **77**(4), 651–659 (1972). doi:10.1029/JA077i004p00651
11. Denton, M.H., Thomsen, M.F., Korth, H., Lynch, S., Zhang, J.C., Liemohn, M.W.: Bulk plasma properties at geosynchronous orbit. J. Geophys. Res. **110**(A7) (2005). doi:10.1029/2004JA010861
12. Draine, B.T., Salpeter, E.E.: On the physics of dust grains in hot gas. Astrophys. J. **231**(1), 77–94 (1979)
13. Garrett, H.B.: The charging of spacecraft surfaces. Rev. Geophys. Space Phys. **19**(4), 577–616 (1981)
14. Hogan, E.: Schaub H (2012a) Space debris reorbiting using electrostatic actuation. In: AAS Guidance and Control Conference, Paper AAS 12–016, Breckenridge
15. Hogan, E., Schaub, H.: Relative motion control for two-spacecraft electrostatic orbit corrections. AIAA J. Guid. Control. Dyn. **36**(1), 240–249 (2013)
16. Hogan, E.A., Schaub, H.: Attitude parameter inspired descriptions of relative orbital motion. In: AIAA/AAS Astrodynamics Specialist Conference, Minneapolis (2012)
17. Jehn, R., Hernandez, C.: International practices to protect the geostationary ring. Space Debris **1**, 221–233 (2001)
18. Katz, I., Davis, V., Snyder, D.B.: Mechanism for spacecraft charging initiated destruction of solar arrays in geo. In: 36th AIAA Aerospace Sciences Meeting and Exhibit, AIAA (1998). doi:10.2514/6.1998-1002
19. King, L.B., Parker, G.G., Deshmukh, S., Chong, J.H.: Spacecraft formation-flying using inter-vehicle coulomb forces. Tech. rep., NASA/NIAC, http://www.niac.usra.edu ((January 2002))
20. Lai, S.T.: An overview of electron and ion beam effects in charging and discharging of spacecraft. IEEE Trans. Nucl. Sci. **36**(6), 2027–2032 (1989)
21. Mullen, E.G., Gussenhoven, M.S., Hardy, D.A.: Scatha survey of high-voltage spacecraft charging in sunlight. J. Geophys. Sci. **91**, 1074–1090 (1986)
22. Murdoch, N., Izzo, D., Bombardelli, C., Carnelli, I., Hilgers, A., Rodgers, D.: Electrostatic tractor for near earth object deflection. In: 59th International Astronautical Congress, vol. 29, Glasgow (2008)
23. Neubert, T., Banks, P.M.: Recent results from studies of electron beam phenomena in space plasmas. Planet. Space Sci. **40**(2/3), 153–183 (1992)
24. Purvis, C.K., Garrett, H.B., Whittlesey, A., Stevens, N.J.: Design guidelines for assessing and controlling spacecraft charging effects, vol. 2361. National Aeronautics and Space Administration, Scientific and Technical Information Branch (1984)
25. Schaub, H., Jasper, L.E.Z.: Circular orbit radius control using electrostatic actuation for 2-craft configurations. In: AAS/AIAA Astrodynamics Specialist Conference, Paper AAS 11–498, Girdwood (2011)

26. Schaub, H., Jasper, L.E.Z.: Orbit boosting maneuvers for two-craft coulomb formations. AIAA J. Guid. Control. Dyn. **36**(1), 74–82 (2013)
27. Schaub, H., Junkins, J.L. Analytical Mechanics of Space Systems, 2nd edn. AIAA Education Series, Reston (2009)
28. Schaub, H., Moorer, D.F.: Geosynchronous large debris reorbiter: Challenges and prospects. J. Astronaut. Sci. **59**(1&2), 165–180 (2012)
29. Schaub, H., Sternovský, Z.: Active space debris charging for contactless electrostatic disposal maneuvers. In: 6th European Conference on Space Debris, ESOC, paper No. 6b.O-5, Darmstadt (2013)
30. Schaub, H.: Stevenson D (2012) Prospects of relative attitude control using coulomb actuation. In: Jer-Nan Juang Astrodynamics Symposium, Paper AAS 12–607, College Station
31. Slisko, J., Brito-Orta, R.A.: On approximate formulas for the electrostatic force between two conducting spheres. Am. J. Phys. **1998**(4), 352–355 (2007)
32. Smythe, W.R. Static and Dynamic Electricity, 3rd edn, McGraw-Hill (1968)
33. Stevenson, D., Schaub, H.: Multi-sphere method for modeling electrostatic forces and torques. Adv. Space Res. **51**(1), 10–20 (2013). doi:10.1016/j.asr.2012.08.014
34. Stevenson, D., Schaub, H.: Rotational testbed for coulomb induced spacecraft attitude control. In: 5th International Conference on Spacecraft Formation Flying Missions and Technologies, Munich (2013)
35. Stiles, L.A., Seubert, C.R., Schaub, H.: Effective coulomb force modeling in a space environment. In: AAS Spaceflight Mechanics Meeting, Paper AAS 12, Charleston (2012)